RSC Advances

PAPER

View Article Online
View Journal | View Issue

Cite this: *RSC Adv.*, 2025, **15**, 15738

Complex interplay of surface properties in modulating antibacterial activity of Ti50Zr alloys†

Alexandra Constantinescu, Camelia Ungureanu, Cristina Dumitriu and Cristian Pirvu *

This study investigates the antibacterial performance of Ti50Zr alloys modified by anodization and ZnO coating, emphasizing the complex interplay of surface properties that influence bacterial inhibition. Three surface morphologies were created *via* anodization: compact oxide (CO), nanotube (NT), and nanochannels (NC). The antibacterial activity of the modified surfaces was evaluated against *Escherichia coli* using inhibition rates and bactericidal ratios. The results showed that surface roughness and morphology significantly affected antibacterial efficiency, with the Ti50Zr NC structure exhibiting the highest inhibition rate (60%). ZnO coating further enhanced antibacterial activity, particularly with Ti50Zr NCZnO, which showed the best performance (75% inhibition). Additionally, Ti50Zr NTZnO demonstrated a significant improvement in antibacterial efficiency, with ZnO nanoparticles (10 nm) playing a key role in membrane penetration. The study also examined the impact of surface energy, wettability, and electrochemical properties on bacterial adhesion and killing mechanisms. These findings underscore the critical influence of surface nanostructuring, ZnO nanoparticle size, and coating on enhancing the antibacterial properties of Ti50Zr, highlighting the complexity of surface interactions in optimizing biomaterials for medical applications.

Received 27th March 2025
Accepted 6th May 2025

DOI: 10.1039/d5ra01182e

rsc.li/rsc-advances

Introduction

Microbe adhesion and colonization on implant surfaces are the most common health-care concerns that negatively affect patient quality of life.[1] The most prevalent pathogens are Gram-positive bacteria such as *Staphylococcus aureus* (*S. aureus*), Gram-negative bacteria as *Escherichia coli* (*E. coli*), and yeasts such as *Candida* spp.[2] *E. coli*, used as a model bacterium in this study, has been extensively investigated for its ability to form biofilms on a variety of surfaces.[3–5] Biofilm formation is a characteristic behaviour of many bacteria, allowing them to adhere to hydrated surfaces.[6]

Surface properties such as hydrophilicity, surface energy, surface charge, roughness, and morphology play a critical role in determining bacterial interactions with implant surfaces. Studies have shown that increasing surface hydrophilicity leads to lower initial bacterial adhesion.[7] Additionally, significant differences in surface energy compared to the microorganism's cell wall enhance antibacterial properties.[7] *E. coli*, like most bacterial cells, carries a negative electric charge, making negatively charged surfaces more effective at repelling these bacteria, which produce polyanionic glycosides.[7] Furthermore, bactericidal effectiveness is significantly enhanced on rough surfaces, particularly those with roughness greater than 20 nm, whereas smooth surfaces exhibit minimal antibacterial effects.[7] The surface morphology can be easily tailored to allow a wide range of topographies, from compact oxide to porous and rough structures such as nanotubes and nanochannels.[8] However, surface nanostructuration does not always guarantee an improved antibacterial response.[9] Surface topography is considered very important in the logarithmic phase of *E. coli* growth[7,10] as bacteria can detect mechanical signals linked to surfaces.[11] Thus, nanoscale topography can influence bacterial attachment through mechanisms involving chemical gradients, physicochemical forces, and cell membrane degradation.[11]

Surface modification strategies, particularly through nanopatterning and the incorporation of antimicrobial compounds, offer promising alternatives to traditional antibiotic treatments by limiting bacterial adhesion.[7] Zinc oxide (ZnO) has garnered significant attention for its antimicrobial properties and its potential for application in biofilm prevention. ZnO is FDA-approved, biocompatible, non-toxic, and exhibits self-cleaning properties.[12–14] Despite its known antimicrobial potential, challenges remain regarding its efficacy against *E. coli* under certain conditions, particularly due to the bacterium's complex cell wall structure, which can make penetration difficult.[15–17]

While much research has focused on microbial colonization on implant surfaces, the comprehensive interaction between the complex surface features of biomaterials and pathogens has

The National University of Science and Technology POLITEHNICA Bucharest, 313 Splaiul Independentei, 060042 Bucharest, Romania. E-mail: cristian.pirvu@upb.ro

† Electronic supplementary information (ESI) available. See DOI: https://doi.org/10.1039/d5ra01182e

not been fully explored. The aim of this study is to adopt a cross-sectional approach to investigate the influence of multiple surface parameters on bacterial sessile behaviour, rather than focusing on a single surface characteristic. For this purpose, TiZr alloy, known for its superior mechanical properties and corrosion resistance in biological fluids compared to commercially pure titanium (cp-Ti), was chosen as the model material. The maximum Zr content for favourable effects was found to be 50%.[8]

In this study, the surface of Ti50Zr alloy was modified in two steps to investigate the complex interaction between physico-chemical and topographical surface features and antibacterial activity against *E. coli*. In the first step, the surface morphology was altered by creating oxide structures such as nanotubes and nanochannels. A comparison was made with native and compact oxide layers. In the second step, ZnO, a bactericidal compound, was deposited on the nanostructured surfaces in various morphologies (rods, nanoparticles, and nanorods). The goal of this second modification was to examine how the properties of ZnO influence the surface characteristics of the nanostructured oxide and, subsequently, the antibacterial efficiency. Given that titanium alloy surface modification inherently involves changes to various surface parameters, this study aims to identify which factors are most critical in improving antibacterial performance.

Experimental

Materials and reagents

Titanium-50-zirconium (Ti50Zr) alloy plates with thicknesses of 2 mm and dimensions of 1.5×1.5 cm^2 [Alfa Aesar] were used in this study. Reagents used to modify the alloy surface: H_2SO_4 [Alfa Aesar] for the compact oxide (CO), NH_4F and $(NH_4)_2SO_4$ [Sigma Aldrich] for nanotubes (NT) and K_2HPO_4 [Alfa Aesar], glycerol, HNO_3 and HF [Sigma Aldrich] for nanochannels (NC) preparation. Zinc electrodeposition was performed in a $Zn(NO_3)_2 \cdot 6H_2O$ [Sigma Aldrich]. NaCl [Sigma Aldrich] was used for electrochemical characterization. For ultrapure water, Direct-Q UV3 [Millipore, USA] was used.

Substrate coating protocol

The Ti50Zr alloy was polished using Beta 2 grinder-polisher with abrasive paper [CarbiMet from Buehler] in different granulations (P 350; P 800; P 1200). The next step involves cleaning and ultrasonication in a Transsonic Ti-H-5 bath for 15 minutes in water, ethanol and acetone.

To obtain the CO surface, the sample was anodized in a 1 M H_2SO_4 solution, at 15 V, for 15 minutes. The sample was called Ti50Zr CO. The sample Ti50Zr NT was obtained by anodization in aqueous electrolyte solution consisting of 0.5% (wt/v) NH_4F and 1 M $(NH_4)_2SO_4$ at 20 V, for 2 h. To obtain Ti50Zr NC sample, the anodization was performed in hot electrolyte as described in a previous study.[18] All anodization processes were carried out with MATRIX power source, model MPS-7163, and a Pt plate as a counter electrode.

Zn was electrodeposited at different temperatures in an aqueous solution of $Zn(NO_3)_2 \cdot 6H_2O$ using an Autolab PGSTAT 302N potentiostat and Nova 1.11 software. Ti50Zr, Ti50Zr CO, Ti50Zr NT, and Ti50Zr NC were used as working electrodes. A Pt rod was used as counter electrode and Ag/AgCl, 3 M KCl as reference electrode. The electrodeposited Zn coating was then oxidized to ZnO by calcination for 1 h at 450 °C in the oven Daihan Labtech model LEF-1035.

The resulted samples were named: Ti50Zr ZnO, Ti50Zr COZnO, Ti50Zr NTZnO and Ti50Zr NCZnO.

Surface characterization

SEM images were obtained with FEI Quanta 650 FEG (field emission gun) from Thermo Scientific, USA. Oxford X-max 80 SDD (Thermo Fisher Scientific) was used for energy-dispersive X-ray (EDX) analysis.

The Atomic Force Microscopy (AFM) was carried out using an A100-SGS microscope (APE Research, Italy). A silicone cantilever from MikroMasch (Estonia) was used for the contact mode AFM analysis. The tip is covered by a Ti layer of 15 nm thickness (the first layer) and a 10 nm layer of Pt (the second layer). For image analysis Gwyddion software was used. Using the three-dimensional image AFM row micrographs and Scanning Probe Image Processor (SPIP 4.6.0) software, the surface parameters, including root mean square roughness (R_{ms}), skewness (S_{sk}), kurtosis (S_{ku}), surface area ratio (S_{dr}) *etc.*, were computed.

The contact angle measurements were performed by the "sessile drop" method using Optical Contact Angle CAM 100 (KSV Instruments, Espoo, FIN). Fluids having different polarities were chosen for contact angle measurements: distilled water, ethylene glycol (EG), and dimethyl sulfoxide (DMSO) from Sigma-Aldrich. Surface energy was calculated according with Owens, Wendt, Rabel (OWRK) method. The surface free energy of the three types of liquids used for this paper was calculated using the Owens–Wendt–Rabel–Kaelble (OWRK) model. The sessile-drop goniometry method was used to measure the contact angle. The values of surface tension of the probe liquids for water, EG and DMSO are 72.8, 48.3 and 44 mN m^{-1} respectively. The measurement was made after 5 seconds from the contact between the drop and the surface to provide a stabilization time. Using a Hamilton syringe, a little amount of liquid, about 3–5 μL, was created and applied to the surface.

An ultra-high UV/Vis/NIR performance spectrophotometer (LAMBDA 950 from PerkinElmer) fitted with a integrating sphere was used to capture the absorbance spectra, which covered the spectral range of 300–800 nm. Recorded spectra were used to obtain Tauc plot according to equations descried in literature.[19,20] A proper extrapolation (PE) as the drawing of a perpendicular from the intersection of the Tauc linear fit and the baseline was used.

Metal ion release was performed in conditions of constant temperature and humidity, ensured by the work in the atmosphere free of contaminants in a clean enclosure of type ISO Class 7.1% HNO_3 in distilled water was used as a blank. The concentration of Zn metallic ions was monitored after 18 hours

of immersion in 0.9% NaCl. The determinations were performed using an Elan DRC-e ICP/MS System (Inductively Coupled Plasma Mass Spectrometer) from PerkinElmer SCIEX U.S.A. with a detection limit of 0.001 μg g^{-1}. Calibration curves for each element were plotted using multi-element standards of 10 mg L^{-1} concentration.

Evaluation of the antimicrobial effect

The antimicrobial effect was tested against Gram-negative bacterium strain, *Escherichia coli* ATCC 8738 using two methods:

(1) Growth rate inhibition (I, %), a quantitative liquid medium testing method was selected for the antibacterial tests, as the solid medium could not accommodate the samples due to their size and weight. Briefly, *E. coli* was grown on autoclaved Luria Bertani Agar (LBA) acc. Miller plates[21] at 37 °C. The sterile samples were incubated for 18 hours in 5 mL of Luria–Bertani broth (the sterile medium was inoculated with bacteria (1%, 0.860×10^5 CFU mL^{-1})) in a Laboshake Gerhardt shaker at 37 °C and 200 rpm. The bacterial growth was determined by measuring optical density for the samples and control (bacterium culture without sample) at 600 nm using UV-Vis spectrophotometer (Jenway Spectrophotometer). Antibacterial activity of all samples against test bacterium were evaluated by a quantitative method, the percentage inhibition of growth, I%.[22]

(2) Bactericidal ratio assay (R, %). A volume of 4 μL of bacterial suspension (0.860×10^5 CFU mL^{-1} in Luria Bertani medium (LB)) was carefully dispensed onto each of the samples under evaluation. After an exposure time of 3 hours, the samples were transferred into a sterile water solution with a volume of 10 mL. Subsequently, the bacterial cells were collected by employing a vigorous vortexing technique on the mixture. A volume of 1 mL of each rinse was put onto LBA plates. To achieve the objective of quantifying the number of bacterial colonies in terms of colony-forming units (CFUs), the Petri dishes were subjected to an incubation period of 18 hours at a temperature of 37 °C (Thermoshaker).[23] The bactericidal ratio (R, %) was calculated as follows:

$$R\ (\%) = \frac{\mathrm{CFU}_{\text{control sample}} - \mathrm{CFU}_{\text{experimental sample}}}{\mathrm{CFU}_{\text{control sample}}} \times 100 \qquad (1)$$

All data were collected in triplicate ($n = 3$) for each experimental group. To evaluate whether the differences in antibacterial activity among the various surface modifications were statistically significant, a one-way analysis of variance (ANOVA) was performed using Microsoft Excel 365, *via* the Data Analysis ToolPak add-in. The significance threshold was set at $\alpha = 0.05$.

Following ANOVA, Tukey's Honest Significant Difference (HSD) post-hoc test was conducted to identify which specific groups exhibited statistically significant differences, while correcting for the family-wise error rate due to multiple comparisons.

Graphical representation of the CFU values included mean values, standard deviation (SD) bars, and significance indicators (** for $p < 0.01$). Statistical results are summarized in the main text and figures.

Results and discussion

Ti50Zr surface modification

Ti50Zr anodization. In the first step, the surface of Ti50Zr was modified by anodization under various conditions to obtain three distinct oxide morphologies: compact oxide, nanotubes, and nanochannels.

For Ti50Zr CO, SEM images reveal a dense, homogeneous, and compact oxide layer with a thickness of approximately 0.6 μm, exhibiting no cracks, Fig. 1a–c.

The Ti50Zr NT sample, as shown in the top view and cross-sectional SEM images (Fig. 1d–f), reveals well-defined, vertically aligned nanotubes. These nanotubes are uniformly distributed across the surface, with an open-top morphology and no nanograss. The tubes have an average diameter of about 75 nm, a length of approximately 6 μm, and a characteristic bamboo-like structure. According to Kim *et al.*, the Zr content in TiZr alloys does not significantly affect the nanotube diameter but can increase the inter-tube spacing.[24] In this study, the inter-tube spacing of the NTs ranged from 90 nm to 130 nm, which is consistent with previously reported values for TiZr alloys with around 40% Zr content.[24]

The morphology of the Ti50Zr NC sample is shown in Fig. 1g–i. Here, one-dimensional (1D) nanochannels with a high aspect ratio are observed. These channels exhibit a sharp appearance, are self-ordered, and grow perpendicularly to the substrate. The nanochannels have open-top pores with diameters ranging from 17 to 34 nm and a length of about 300 nm.

Electrodeposition of ZnO. In the second step, Zn was electrodeposited onto Ti50Zr modified surfaces *via* cathodic

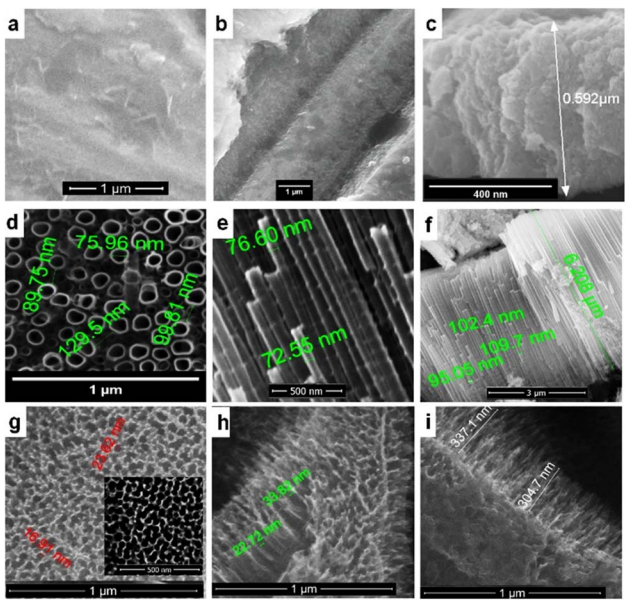

Fig. 1 SEM images of the top (a), (d) and (g) and cross-sectional (b), (c), (e), (f), (h) and (i) view for Ti50Zr CO (a)–(c), Ti50Zr NT (d)–(f) and Ti50Zr NC (g)–(i).

polarization. To determine the optimal deposition potential, voltammograms were recorded between +0.7 V and −2 V (Fig. S1†) in NaCl 0.9% and NaCl 0.9% + $Zn(NO_3)_2$ electrolytes for both unmodified and anodized TiZr samples. Zinc reduction started between −1.3 V and −1.5 V for all samples.

Several parameters were varied to optimize the electrodeposition process: temperature (60 °C, 70 °C, 80 °C), electrolyte concentration (5 mM, 10 mM, 15 mM), cathodic potential (−1.3 V, −1.4 V, −1.5 V), and pulse number (90, 150, 200). The best results were achieved using a deposition scheme with a brief initial polarization at −2 V (2 s) for zinc nucleation, followed by a pulse cycle of 0 V for 5 s, then −1.4 V for 2 s, repeated 150 times (Fig. 2a). A 10 mM aqueous solution of $Zn(NO_3)_2$ at 70 °C was used for all samples. The corresponding cathodic and anodic current profiles during the electrochemical deposition are shown in Fig. 2.

For Ti50Zr sample, the cathodic charge (corresponding to the −1.4 V pulse) increased linearly to 4.52C, while the anodic charge (corresponding to the 0 V pulse) reached 2.69C. The larger cathodic charge (a difference of 1.83C) indicates that zinc deposition is predominant over the oxidation. Some reduction of the native oxide (*e.g.*, Ti^{4+} to Ti^{3+}) may also occur, as suggested by the Pourbaix diagram. SEM images after annealing revealed a uniform ZnO layer with particles in hexagonal or irregular shapes, around 80 nm in diameter, covering the entire surface (Fig. 3a–c).

For Zn electrodeposition on the Ti50Zr CO surface, the charge increase was non-linear, and a smaller difference between the cathodic and anodic charge (0.64C) was observed. SEM images showed predominantly hexagonal ZnO rods (with a 120° angle) and particles ranging from 195–235 nm, with partial coverage of the substrate (Fig. 3f).

For Ti50Zr NT, the deposition graph showed nearly symmetrical current branches, with the total charge reaching 6C. Zinc formed a thin film on the nanotube walls, increasing the tube diameter from 75 nm to ~82 nm, with small nanoparticles (~10 nm) observed in the interspaces.

On the Ti50Zr NC surface, the extra cathodic charge resulted in partial coverage with ZnO nanorods (80 nm), as shown in SEM (Fig. 3j–l).

EDX spectra (Table S1†) showed that the oxide composition generally matched the alloy ratio, with small variations. For the untreated Ti50Zr, the Ti/Zr ratio was 1.3, with Ti present in a higher percentage. Jairo M. Cordeiro and Co. made similar observations for other TiZr alloys.[25] A possible explanation being the lower equilibrium oxygen partial pressure at the Zr/ZrO_2 interface compared to that at the Ti/TiO_2 interface, as shown by the Ellingham–Richardson diagram.[26]

Zn content was lowest on Ti50Zr NC (1.11%) and Ti50Zr NT (2.97%), compared to the native oxide (33.4%) and Ti50Zr CO (36.53%).

This confirms that ZnO morphology and content are influenced by the underlying substrate morphology.

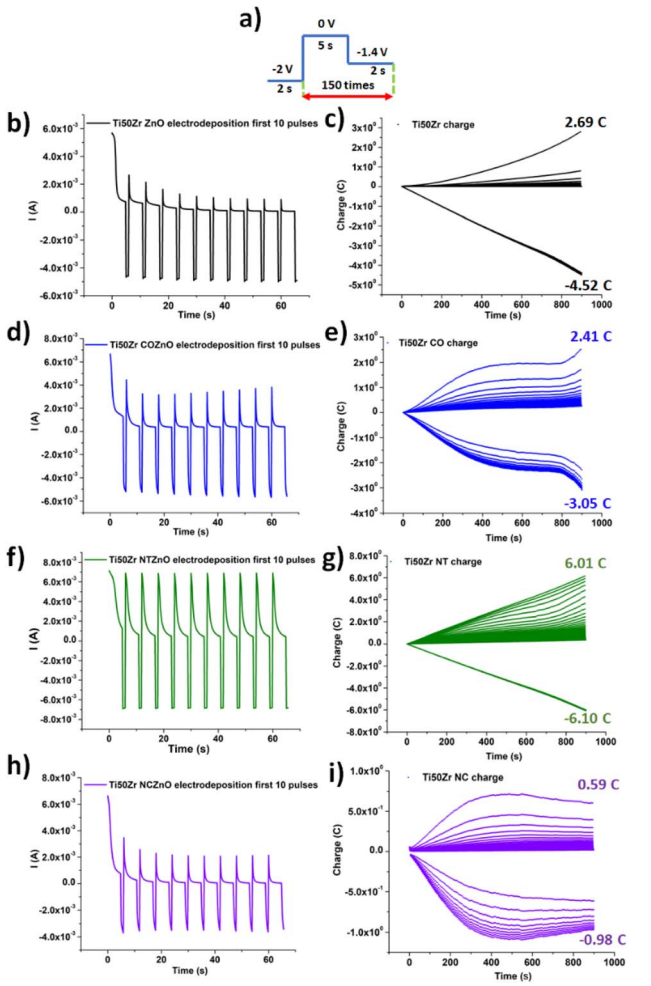

Fig. 2 Pulse deposition scheme (a), current–time diagrams corresponding to pulsed ZnO electrodeposition, first ten pulses (b), (d), (f) and (h) and charge–time diagrams (c), (e), (g) and (i).

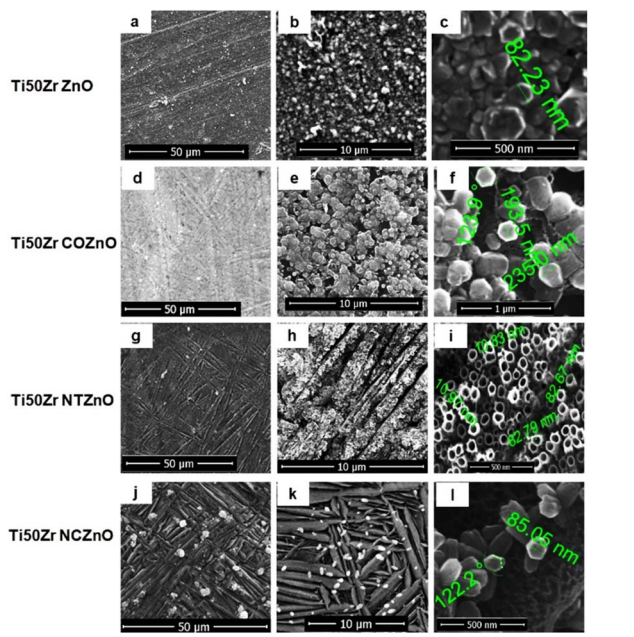

Fig. 3 SEM images at different magnifications corresponding to: (a)–(c) Ti50Zr ZnO; (d)–(f) Ti50Zr COZnO; (g)–(i) Ti50Zr NTZnO; (j)–(l) Ti50Zr NCZnO.

Samples characterization

Contact angle and surface energy. Table 1 shows the contact angle (CA) and surface energy values for three liquids (water, DMSO, and EG). The Ti50Zr substrate is nearly hydrophobic with a water contact angle around 90°. Surface modification with CO slightly increased hydrophilicity (contact angle 74° compared to 80°), while nanostructuration (NT and NC) made the surface more hydrophilic (25° and 32°, respectively).

ZnO deposition generally increased the water contact angle, making most samples hydrophobic or close to hydrophobic: Ti50Zr (from 80° to 85°), Ti50Zr CO (from 74° to 103°), and Ti50Zr NC (from 32° to 110°). The exception was Ti50Zr NTZnO, where the contact angle change was minimal (from 25° to 28°), likely due to the ZnO nanoparticle arrangement on the nanotube walls and interspaces, which may not be fully wetted. Ti50Zr NCZnO showed increased contact angles for water, EG, and DMSO, indicating a more complex surface structure sustained by the highest value of S_{dr} from AFM analysis (Table S5†) than simple changes in the surface polarity. The standard deviation (SD) of each parameter was calculated (Table 1).

CO surfaces exhibited the lowest variability, confirming their homogeneous and stable wettability properties. Ti50Zr CO recorded an $SD_{WaterCA}$ of 0.14°, 0.35° (EG), and 1.04° (DMSO), while Ti50Zr COZnO presented comparable values, indicating that ZnO modification had minimal impact on uniformity, except for a slight increase in EG variability.

NT surfaces also demonstrated low SD, ensuring reproducible liquid interactions. Ti50Zr NT recorded 0.11° (water), 0.26° (EG), and 0.45° (DMSO), while ZnO-modified Ti50Zr NTZnO further reduced EG variability to 0.05°, highlighting the stabilizing effect of ZnO on polar liquid interactions.

In contrast, NC surfaces showed the highest variability, indicating significant surface heterogeneity. Ti50Zr NC exhibited an $SD_{WaterCA}$ of 3.05°, 1.06° (EG), and 0.08° (DMSO), suggesting irregular surface topography. ZnO modification (Ti50Zr NCZnO) reduced $SD_{WaterCA}$ (0.53°) but increased dispersion in DMSO (3.96°), emphasizing the disruptive impact of ZnO on non-polar liquid spreading.

Overall, CO and NT surfaces demonstrated the most consistent wettability, making them suitable for applications requiring stable and predictable surface interactions, while NC surfaces exhibited higher variability, which may be advantageous for dynamic wettability applications. ZnO modification altered surface energy, affecting variability differently depending on the liquid, with improved uniformity in some cases (EG on NTZnO) and increased heterogeneity in others (DMSO on NCZnO).

Surface energy, important for bio applications, was highest for Ti50Zr NT and Ti50Zr NC (66 and 61 mJ m^{-2}, respectively). ZnO deposition increased surface energy in all cases, with the highest value (76 mJ m^{-2}) observed for Ti50Zr NCZnO, where ZnO raised the surface energy by 15 mJ m^{-2}. The Zn content for Ti50Zr NCZnO was 1.11%. For Ti50Zr NTZnO, ZnO deposition as nanoparticles slightly increased surface energy from 66 to 68 mJ m^{-2}, with a Zn content of 2.97%. Surface energy appears strongly influenced by morphology, with NC and ZnO nanorods having a greater impact compared to NT and ZnO nanoparticles.

These results provide valuable insights into the wettability behaviour of Ti50Zr-based surfaces, emphasizing the role of nanostructuring and ZnO integration in controlling liquid–surface interactions, which is crucial for applications in biomedicine.

AFM analysis. Fig. 4 presents AFM 3D images of all tested samples. Table S5† presents AFM parameters (S_{sk}, S_{ku}, R_{ms}, S_{dr}) for all samples. After the first surface modification step, polished Ti50Zr showed low roughness, which decreased further after CO deposition. Nanostructured samples, Ti50Zr NT and Ti50Zr NC exhibited increased roughness, from 0.085 μm for Ti50Zr to 0.225 μm for Ti50Zr NT and 0.352 μm for Ti50Zr NC. The surface area ratio (S_{dr}) also increased, from 0.85% for Ti50Zr to 2.41% for Ti50Zr NT and 17.99% for Ti50Zr NC. This increase in roughness and S_{dr} corresponds to greater hydrophilicity, with Wenzel's model applying to Ti50Zr NT and Ti50Zr NC. However, Ti50Zr NC, despite having the highest roughness and S_{dr}, was less hydrophilic than Ti50Zr NT, suggesting a possible intermediate state. Higher roughness and hydrophilicity benefit osteogenic cell migration, making Ti50Zr NT and Ti50Zr NC suitable for implant modifications. The sharpness of Ti50Zr NC's nanochannel structures is confirmed by the Kurtosis value ($S_{ku} > 3$), with Ti50Zr NC showing a S_{ku} of 4.59 and Ti50Zr NT a S_{ku} of 2.34.

After the second modification step, the water contact angle for Ti50Zr increased from 80° to 85° as roughness (R_{ms}) rose from 0.085 to 0.929 μm. A similar trend was observed for Ti50Zr COZnO. The increase in contact angle with roughness suggests

Table 1 Values of the contact angle, standard deviation and surface energy of Ti50Zr substrate and coated samples

Sample	Contact angle mean (°) ± standard deviation (°)			Surface energy (mJ m^{-2} or mN m^{-1})
	Water	Ethylene glycol	DMSO	
Ti50Zr	80 ± 1.18	41 ± 0.23	30 ± 1.02	40
Ti50Zr ZnO	85 ± 0.64	19 ± 0.68	10 ± 0.31	54
Ti50Zr CO	74 ± 0.14	36 ± 0.35	30 ± 1.04	40
Ti50Zr COZnO	103 ± 0.13	39 ± 0.69	11 ± 0.13	56
Ti50Zr NT	25 ± 0.11	15 ± 0.26	10 ± 0.45	66
Ti50Zr NTZnO	28 ± 0.24	8 ± 0.05	4 ± 0.73	68
Ti50Zr NC	32 ± 3.05	12 ± 0.16	10 ± 0.08	61
Ti50Zr NCZnO	110 ± 0.53	48 ± 0.68	22 ± 3.96	76

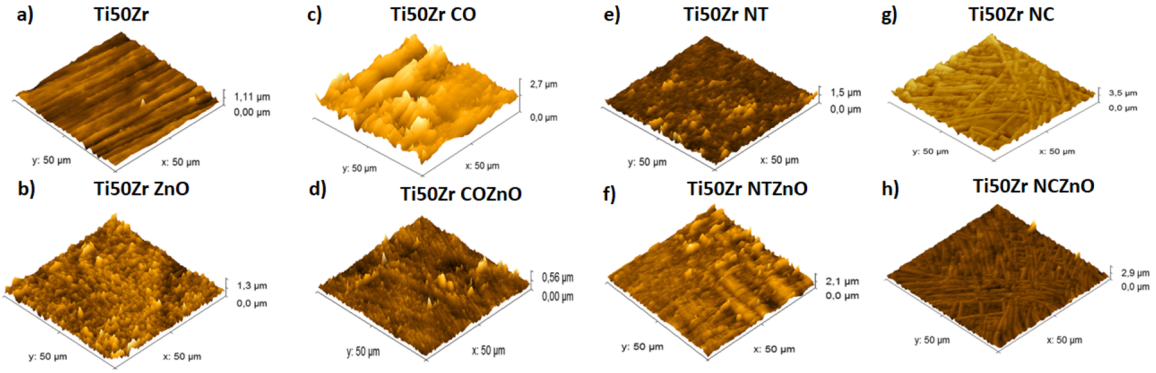

Fig. 4 AFM 3D images and roughness values for: (a) Ti50Zr (b) Ti50Zr ZnO (c) Ti50Zr CO (d) Ti50Zr COZnO (e) Ti50Zr NT and (f) Ti50Zr NTZnO (g) Ti50Zr NC (h) Ti50Zr NCZnO.

an intermediate state between the Cassie and Wenzel models, known as the 'mushroom state'.

The SD of each parameter was calculated (Table S6†) to assess the variability in surface morphology across different modifications, including compact oxide (CO), nanotube (NT), nanochannel (NC), and ZnO-coated surfaces.

S_{sk} variability. CO surfaces (Ti50Zr CO and Ti50Zr COZnO) exhibited the lowest $SD_{S_{sk}AFM}$ (0.10 and 0.06), indicating highly symmetric and homogeneous surface profiles. Nanochannel (Ti50Zr NC: 0.44) and nanotube (Ti50Zr NTZnO: 0.45) surfaces displayed the highest $SD_{S_{sk}AFM}$, reflecting increased surface asymmetry and irregularities. ZnO modification increased skewness variability, particularly in Ti50Zr ZnO (0.25) and Ti50Zr NCZnO (0.21), likely due to heterogeneous ZnO deposition.

S_{ku} variability. Ti50Zr CO exhibited the lowest $SD_{S_{ku}AFM}$ (0.05), confirming its flat and uniform surface texture. Nanochannel and nanotube surfaces displayed higher $SD_{S_{ku}AFM}$, especially Ti50Zr NTZnO (1.09) and Ti50Zr NCZnO (1.02), suggesting more pronounced peak structures. ZnO-coated surfaces (Ti50Zr ZnO, Ti50Zr NCZnO, Ti50Zr COZnO) exhibited increased kurtosis variability, indicating less uniform peak distributions and higher roughness fluctuations.

R_{ms} variability. CO surfaces (Ti50Zr CO: 0.01 μm) exhibited the lowest $SD_{R_{ms}AFM}$, confirming a highly controlled and smooth surface. ZnO modification significantly increased roughness variability, with Ti50Zr COZnO displaying an SD of 0.45 μm, indicating that ZnO deposition leads to greater roughness fluctuations. Nanochannel (Ti50Zr NC: 0.02 μm) and nanotube (Ti50Zr NT: 0.04 μm) structures also exhibited increased $SD_{R_{ms}AFM}$, reflecting their intrinsically rougher topographies.

***S_{dr}* variability.** Ti50Zr CO exhibited the lowest $SD_{S_{dr}AFM}$ (0.01%), reinforcing its compact, stable, and homogeneous structure. Nanochannel surfaces exhibited the highest $SD_{S_{dr}AFM}$ (Ti50Zr NC: 6.07%), indicating a highly complex and rough topography. ZnO modification increased surface area complexity, particularly in Ti50Zr ZnO (2.58%) and Ti50Zr NTZnO (3.34%), suggesting that ZnO deposition enhances surface texturing and heterogeneity.

CO surfaces exhibited the lowest variability in all parameters, confirming their highly uniform and stable morphology. NC and NT surfaces displayed higher variability in S_{sk}, S_{ku}, R_{ms}, and S_{dr}, reflecting greater roughness, asymmetry, and peak variations. ZnO modification increased roughness and peak variability, especially in Ti50Zr COZnO and Ti50Zr NCZnO, suggesting that ZnO influences surface complexity and heterogeneity. NC surfaces exhibited the highest surface complexity (S_{dr}), making them highly textured and rough.

These results demonstrate the impact of nanostructuring and ZnO modification on roughness and wettability, providing insights into material selection for biomedical applications. ZnO-coated nanotubes suggest greater structural irregularities, which may impact their behaviour in contact with biological environments.

Electrical double layer capacitance. At the biomaterial–electrolyte interface, the relationship between surface charge and the oxide–solution interface influences the double-layer capacitance (C_{dl}), a key characteristic for surface interactions. Previous studies highlight the role of the electrical double layer in bacterial adhesion, as bacterial cell surfaces are typically negatively charged in physiological conditions, which can induce repulsion when approaching negatively charged titanium alloy surfaces.[27]

After the first surface modification step, the growth of the compact oxide layer on Ti50Zr alloy smoothed the surface, reducing the active area and lowering the C_{dl} (Fig. 5a and b). In contrast, nanostructuring Ti50Zr with porous NT improves surface wettability and roughness, enhancing charge transfer and double-layer formation. The increased roughness and porosity in Ti50Zr NT and Ti50Zr NC contribute to higher C_{dl} values, particularly for Ti50Zr NT (5.66 mF cm^{-2}), suggesting more efficient ion adsorption and desorption. Ti50Zr NC, with its higher roughness and S_{dr}, exhibits a lower C_{dl} (2.26 mF cm^{-2}), likely due to smaller nanochannel dimensions and an intermediate surface state between the Cassie and Wenzel models.

In the second modification step, ZnO deposition on the Ti50Zr surface increases C_{dl}, Fig. 5a. This phenomenon is observed in metal oxide coatings,[28] as seen in Ti50Zr CO, where electrochemical pulsed Zn deposition and subsequent ZnO rod formation enhance the active surface and C_{dl} (from 0.11 to 1.2 mF cm^{-2}). However, for Ti50Zr NTZnO and Ti50Zr NCZnO, C_{dl}

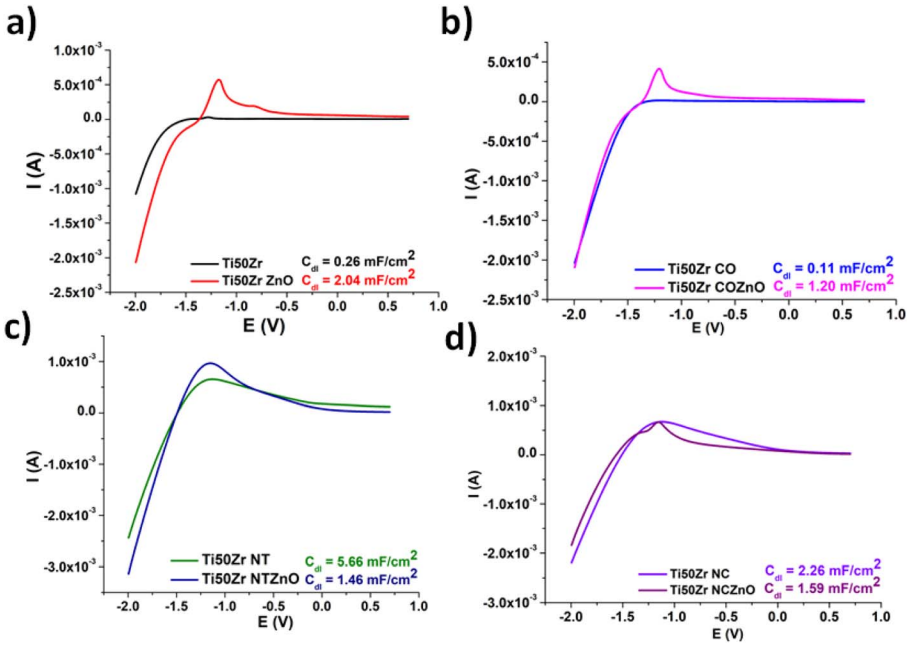

Fig. 5 Anodic branch of the cyclic voltammograms used for C_{dl} calculation, corresponding to (a) Ti50Zr and Ti50Zr ZnO, (b) Ti50Zr CO and Ti50Zr COZnO, (c) Ti50Zr NT and Ti50Zr NTZnO, (d) Ti50Zr NC and Ti50Zr NCZnO.

decreases after ZnO deposition. This reduction is likely due to a decrease in roughness, as shown in the AFM analysis, where ZnO deposition on nanotube walls and interspaces and nanochannels reduces the active surface area.

Zinc ion release. After 18 hours of immersion, ICP-MS analysis showed the following Zn^{2+} ion release concentrations (in ppm): 0.901 for Ti50Zr ZnO, 0.817 for Ti50Zr COZnO, 0.315 for Ti50Zr NTZnO, and 0.483 for Ti50Zr NCZnO. These results correlate with the surface modifications and characteristics of each sample.

Ti50Zr ZnO and Ti50Zr COZnO, which exhibited the highest Zn surface content (36.53% and 33.4%, respectively), released the highest concentrations of Zn^{2+}, indicating a stronger ZnO presence. These samples also showed increased surface energy and hydrophobicity after ZnO deposition, consistent with the enhanced Zn ion release.

In contrast, Ti50Zr NTZnO and Ti50Zr NCZnO, with lower Zn surface content (2.97% and 1.11%, respectively), had lower Zn^{2+} release. This is consistent with the observed decrease in surface roughness after ZnO deposition, which likely reduced the active surface area and, consequently, the ion release.

Antibacterial activity. The antibacterial activity of Ti50Zr samples, modified with different surface structures and coatings, was evaluated using Growth Rate Inhibition and Bactericidal Ratio assays, as described in Experimental. The unmodified Ti50Zr substrate (C*) exhibited the lowest inhibition rate against *E. coli* (20%), as shown in Table 2. Surface modifications significantly enhanced antibacterial properties, with Ti50Zr NC nanostructures (with needle-like features) exhibiting the highest inhibition rate of 60%, a +41% improvement compared to the unmodified substrate. ZnO coatings further boosted the antibacterial effect. Specifically, Ti50Zr NCZnO showed the best antibacterial performance with a 75% inhibition rate, while Ti50Zr NTZnO exhibited a 71% inhibition rate, which represents a +47% increase over Ti50Zr NT. The results obtained through the two methods utilized, are closely aligned in terms of their values.

Literature reported that ZnO NPs has effectively inhibited the *E. coli* growth by 67% (ref. 29) or 56%.[30] However, in a recent study, a greater antibacterial effect was obtained but this was due to the synergistic effect between ZnO nanoparticles and antibiotics.[31]

Ti50Zr surface modification significantly impacted surface characteristics such as hydrophilicity, surface energy, roughness, and capacitance (C_{dl}), which influence bacterial adhesion. As summarized in Table 3, Ti50Zr NT, which had the highest surface energy and hydrophilicity, did not exhibit a large improvement in antibacterial efficiency (24% inhibition rate, 25% bactericidal ratio). Conversely, Ti50Zr NC, with a less hydrophilic surface and lower surface energy (61 mJ m^{-2}), showed the highest antibacterial efficiency, with a 60%

Table 2 Antibacterial activity. Inhibition rate (%) and bactericidal ratio (%)

Sample	Inhibition rate (%)	Bactericidal ratio (%)
Ti50Zr	C*	C*
Ti50Zr ZnO	57	56
Ti50Zr CO	20	21
Ti50Zr COZnO	54	55
Ti50Zr NT	24	25
Ti50Zr NTZnO	71	70
Ti50Zr NC	60	63
Ti50Zr NCZnO	75	77

Table 3 Comparative features of anodized samples (Ti50Zr CO, Ti50Zr NT and Ti50Zr NC) *versus* Ti50Zr substrate[a]

Features	Ti50Zr CO *vs.* Ti50Zr	Ti50Zr NT *vs.* Ti50Zr	Ti50Zr NC *vs.* Ti50Zr
Hydrophilicity	Slightly more hydrophilic (+)	More hydrophilic (+++)	More hydrophilic (++)
Surface energy	The same (=)	Higher (++)	Higher (+)
Roughness (R_{ms})	Lower (−)	Higher (+)	Higher (++)
C_{dl}	Lower (−)	Higher (++)	Higher (+)
Morphology (oxide nanostructuration)	Compact oxide	Nanotubes	Nanochannels
Antibacterial efficiency	Slightly higher	Slightly higher	Higher
Inhibition rate, I (%)	(20%)	(24%)	(60%)
Bacetericidal ratio, R (%)	(21%)	(25%)	(63%)

[a] Number of (+)/(−) indicates the increase/decrease order of the parameters compared to the reference sample. (=) means similar values.

inhibition rate and a 63% bactericidal ratio, suggesting that surface roughness and morphology (sharp, high aspect ratio nanostructures) are more critical than hydrophilicity in promoting antibacterial activity. The sharp nanochannel structure of Ti50Zr NC likely penetrates bacterial membranes, causing oxidative stress and mechanical damage, leading to enhanced antibacterial performance.

ZnO deposition further influenced antibacterial activity, with ZnO applied in different morphologies depending on the underlying surface structure. As seen in Table 4, Ti50Zr NTZnO, with ZnO nanoparticles (~10 nm), showed the greatest increase in antibacterial efficiency (+47%), while Ti50Zr NCZnO, with ZnO nanorods (~80 nm), showed a more modest increase (+15%). ZnO's antibacterial effect is attributed to several mechanisms, including electrostatic interaction, Zn^{2+} ion release, and the potential generation of reactive oxygen species (ROS). Thus, the antibacterial performance of Ti50Zr alloys is influenced by a combination of electronic properties, surface morphology, and ZnO nanoparticle characteristics. While the band gap and band-edge properties, as shown in Fig. S2 and Table S2,† support ROS generation, their impact appears secondary to morphological and mechanical factors. Enhanced antibacterial efficiency is primarily driven by features such as increased roughness, sharp nanostructures enabling membrane penetration, and the activity of small ZnO nanoparticles, which maximize bacterial contact and disruption. Despite Ti50Zr NTZnO having the lowest ZnO surface content and Zn^{2+} ion release (1.37×10^{-5} mol L^{-1}), it showed the most significant improvement in antibacterial efficiency, highlighting that surface morphology specifically, the presence of small ZnO nanoparticles can be a more important factor than the amount of ZnO present or the surface energy.

Table 4 also shows that Ti50Zr ZnO and Ti50Zr COZnO exhibited similar antibacterial efficiencies (+38% and +34%, respectively), while Ti50Zr NCZnO had a smaller improvement in antibacterial performance. This suggests that a combination of surface morphology from the first modification step and ZnO deposition from the second modification step plays a significant role in enhancing antibacterial activity, with sharp nanostructures enabling more effective bacterial inhibition.

Statistically, as shown in Fig. 6, the CFU values varied notably between the tested surfaces. The uncoated TiZr control exhibited the highest bacterial adhesion (mean CFU = 522), confirming its limited antibacterial properties.

Among the surface-modified samples, Ti50Zr NCZnO showed the most effective antibacterial behaviour, with a significant CFU reduction (mean = 120 ± 5.7), corresponding to an inhibition rate of approximately 75%. Similarly, Ti50Zr COZnO also demonstrated strong antibacterial effects (mean = 157 ± 1.5). In contrast, samples such as Ti50Zr NTZnO and Ti50Zr ZnO showed moderate CFU reductions but did not differ significantly from the control in statistical terms.

Statistical analysis using one-way ANOVA followed by Tukey's HSD post-hoc test confirmed that surface modification

Table 4 Comparative features of ZnO coated samples *versus* uncoated[a]

Features	Ti50Zr ZnO *vs.* Ti50Zr	Ti50Zr COZnO *vs.* Ti50Zr CO	Ti50Zr NTZnO *vs.* Ti50Zr NT	Ti50Zr NCZnO *vs.* Ti50Zr NC
Hydrophilicity	Slightly less hydrophilic (−−)	Hydrophobic (−−−)	Slightly less hydrophilic (−)	Hydrophobic (−−−−)
Surface energy	Higher (++)	Higher (++++)	Slightly higher (+)	Higher (+++)
Roughness	Higher (++++)	Higher (+++)	Lower (−−)	Lower (−)
C_{dl}	Higher (++)	Higher (+)	Lower (−)	Lower (−−)
Morphology (ZnO nanostructuration)	Nanorods (~80 nm)	Rods (~200 nm)	Nanoparticles (~10 nm)	Nanorods (~80 nm)
Zn surface content (EDS)	(+++)	(++++)	(++)	(+)
Zn^{2+} ion release	(++++)	(+++)	(+)	(++)
Antibacterial efficiency	Higher (+38%)	Higher (+34%)	Higher (+47%)	Higher (+15%)

[a] Number of (+)/(−) indicates the increase/decrease order of the parameters compared to the reference sample.

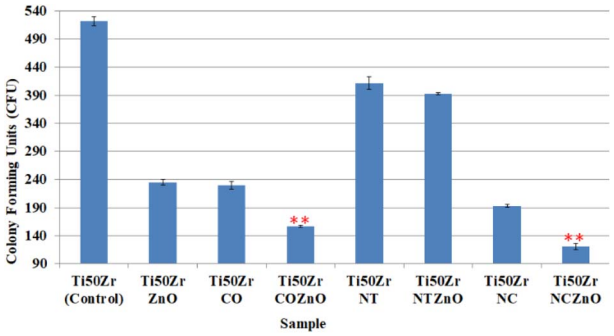

Fig. 6 CFU values SD bars. '**' indicates $p < 0.01$ significance based on Tukey's HSD test.

had a significant impact on bacterial adhesion ($p < 0.0001$). Importantly, only Ti50Zr NCZnO and Ti50Zr COZnO showed statistically significant differences ($p < 0.01$) compared to both the untreated control (Ti50Zr) and anodized-only surfaces such as Ti50Zr NT. These are marked with '**' in Fig. 6.

These results suggest a synergistic effect between nanoscale surface structuring and the presence of ZnO coating. While anodization alone reduced bacterial attachment to some extent, the incorporation of ZnO drastically enhanced antibacterial performance—likely due to the combined effects of Zn^{2+} ion release, reactive oxygen species (ROS) generation, and surface wettability modification.

Overall, Ti50Zr NCZnO and Ti50Zr COZnO are promising candidates for implantable materials where antibacterial performance is critical.

These results, together with the low Zn^{2+} ion release and high corrosion resistance, suggest that the Ti50Zr ZnO coatings are promising for implantable applications. Although not assessed in this study, their cytocompatibility is strongly supported by literature data.[8,13,14] Ionita *et al.* demonstrated that TiZr alloys with similar nanostructures promote osteoblast adhesion and proliferation without cytotoxic effects, making them promising materials for orthopedic applications.[8] Additionally, ZnO has been widely acknowledged as a biocompatible and FDA-approved material, with Al-Mohaimeed *et al.* and Mehrvarz *et al.* reporting excellent cytocompatibility of ZnO coatings in contact with various mammalian cell lines.[13,14] Also, Sirelkhatim *et al.*[17] provided a comprehensive review confirming the biocompatibility and low cytotoxicity of ZnO nanostructures in biological environments. Therefore, based on these findings, it is reasonable to anticipate that the surfaces developed in this work will also exhibit favorable cytocompatibility, supporting their future use in implantable medical devices.

All coated samples have improved electrochemical stability in NaCl 0.9%, with protection efficiency over 50%, sustaining its potential to be used as an implant material (ESI†).

Conclusions

This study provides a comprehensive analysis of the antibacterial performance against *E. Coli* of Ti50Zr alloys modified through anodization and ZnO coating, emphasizing the multifactorial interactions that govern bacterial adhesion and inhibition.

Effect of surface morphology on *E. coli* antibacterial activity

- Anodization resulted in three distinct oxide morphologies: compact oxide (CO), nanotubes (NT), and nanochannels (NC).
- The Ti50Zr NC structure exhibited the highest antibacterial efficiency, with an inhibition rate of 60%, attributed to its high-aspect-ratio nanochannel morphology.
- ZnO coating further enhanced antibacterial activity, with Ti50Zr NCZnO demonstrating the highest inhibition rate (75%), suggesting a synergistic effect between surface nanostructuring and ZnO-mediated bacterial inactivation.

Physicochemical modifications and their impact on antibacterial properties

- Surface roughness, wettability, and surface energy were identified as critical parameters influencing bacterial adhesion and inhibition.
- While increased hydrophilicity generally promotes reduced bacterial adhesion, Ti50Zr NCZnO—despite exhibiting hydrophobic characteristics—showed the highest antibacterial efficiency, indicating that surface morphology plays a dominant role.
- ZnO nanoparticle size significantly influenced antibacterial performance, with Ti50Zr NTZnO (containing ~10 nm ZnO nanoparticles) exhibiting a 47% increase in bacterial inhibition compared to uncoated Ti50Zr NT, highlighting the importance of nanoparticle interaction with bacterial membranes.

Electrochemical properties and ZnO ion release contribution

- The double-layer capacitance (C_{dl}) varied with surface morphology and ZnO deposition, influencing bacterial adhesion mechanisms.
- ZnO-coated samples exhibited distinct Zn^{2+} ion release profiles, with Ti50Zr NTZnO demonstrating the lowest ion release yet the most significant antibacterial enhancement, suggesting that ZnO nanoparticle size and distribution contribute more to antibacterial performance than Zn^{2+} ion concentration alone.
- The antibacterial mechanism is primarily driven by a combination of mechanical disruption (due to surface nanostructuring), ZnO-mediated oxidative stress, and electrostatic interactions rather than a single dominant factor.

The results of this study underscore the importance of surface nanostructuring and ZnO incorporation in enhancing the antibacterial properties of Ti50Zr alloys. The findings highlight the complex interplay between surface morphology, physicochemical properties, and ZnO-mediated bacterial interactions, providing valuable insights for the development of next-generation antibacterial biomaterials for medical applications.

Data availability

The data supporting this article have been included as part of the ESI.†

Author contributions

A. Constantinescu: investigation, validation, formal analysis, writing – original draft, writing – review & editing. C. Ungureanu: methodology, investigation, resources, writing – review & editing. C. Dumitriu: investigation, methodology, writing – original draft. C. Pirvu: conceptualization, methodology, investigation, validation, resources, writing – original draft, writing – review & editing.

Conflicts of interest

There are no conflicts to declare.

References

1 P. Erkoc and F. Ulucan-Karnak, *Prosthesis*, 2021, **3**, 25–52.
2 N. H. Harun, R. B. S. Mydin, S. Sreekantan, K. A. Saharudin, Y. L. Khor, N. Basiron and A. Seeni, *Journal of Biomedical and Clinical Sciences*, 2018, **3**, 75–78.
3 A. Terada, K. Okuyama, M. Nishikawa, S. Tsuneda and M. Hosomi, *Biotechnol. Bioeng.*, 2012, **109**, 1745–1754.
4 S. H. Yoon, N. Rungraeng, W. Song and S. Jun, *J. Food Eng.*, 2014, **131**, 135–141.
5 S. L. Arias, J. Devorkin, A. Civantos and J. P. Allain, *Langmuir*, 2021, **37**, 16–25.
6 S. T. Asma, K. Imre, A. Morar, V. Herman, U. Acaroz, H. Mukhtar, D. Arslan-Acaroz, S. R. A. Shah and R. Gerlach, *Life*, 2022, **12**, 1–31.
7 X.-w. Ji, P.-t. Liu, J.-c. Tang, C.-j. Wan, Y. Yang, Z.-l. Zhao and D.-p. Zhao, *Trans. Nonferrous Met. Soc. China*, 2021, **31**, 3821–3830.
8 D. Ionita, C. Pirvu, A. B. Stoian and I. Demetrescu, *Coatings*, 2020, **10**, 422.
9 J. S. Kun Yang, L. Wang, Y. Chen, C. Liang, L. Yang and L.-N. Wang, *J. Mater. Sci. Technol.*, 2022, **99**, 82–100.
10 Y. H. Leung, X. Xu, A. P. Y. Ma, F. Liu, A. M. C. Ng, Z. Shen, L. A. Gethings, M. Y. Guo, A. B. Djurišić, P. K. H. Lee, H. K. Lee, W. K. Chan and F. C. C. Leung, *Sci. Rep.*, 2016, **6**, 35243.
11 S. Zheng, M. Bawazir, A. Dhall, H.-E. Kim, L. He, J. Heo and G. Hwang, *Frontiers in Bioengineering and Biotechnology*, 2021, **9**, 643722.
12 S. Kavitha, S. Sadishkumar and N. Prabhu, *Int. J. Mech. Eng.*, 2021, **6**, 972–982.
13 A. M. Al-Mohaimeed, W. A. Al-Onazi and M. F. El-Tohamy, *Molecules*, 2022, **27**, 579.
14 A. Mehrvarz, J. Khalil-Allafi and A. K. Khosrowshahi, *Ceram. Int.*, 2022, **48**(11), 16326–16336.
15 P. K. Mishra, H. Mishra, A. Ekielski, S. Talegaonkar and B. Vaidya, *Drug discovery today*, 2017, **22**, 1825–1834.
16 K. Rajendran, M. Gajendiran, S. Kim, K. Kim and S. Balasubramanian, *J. Ind. Eng. Chem.*, 2018, **57**, 387–395.
17 A. Sirelkhatim, S. Mahmud, A. Seeni, N. H. M. Kaus, L. C. Ann, S. K. M. Bakhori, H. Hasan and D. Mohamad, *Nano-Micro Lett.*, 2015, **7**, 219–242.
18 R. Ion, A. B. Stoian, C. Dumitriu, S. Grigorescu, A. Mazare, A. Cimpean, I. Demetrescu and P. Schmuki, *Acta Biomater.*, 2015, **24**, 370–377.
19 A. Z. Johannes, R. K. Pingak and M. Bukit, *IOP Conf. Ser.: Mater. Sci. Eng.*, 2020, **823**, 012030.
20 B. D. Viezbicke, S. Patel, B. E. Davis and D. P. Birnie III, *Phys. Status Solidi B*, 2015, **252**, 1700–1710.
21 M. Ansari, H. M. Khan and A. Khan, *Biol. Med.*, 2011, **3**(2), 141–146.
22 S. Jaiswal, B. Duffy, A. K. Jaiswal, N. Stobie and P. McHale, *Int. J. Antimicrob. Agents*, 2010, **36**, 280–283.
23 M. Grecu, G. Novac, D. Ionita and C. Ungureanu, *Rev. Chim.*, 2011, **62**, 352–356.
24 W.-G. Kim and H.-C. Choe, *Trans. Nonferrous Met. Soc. China*, 2009, **19**, 1005–1008.
25 J. M. Cordeiro, L. P. Faverani, C. R. Grandini, E. C. Rangel, N. C. da Cruz, F. H. Nociti Junior, A. B. Almeida, F. B. Vicente, B. R. G. Morais, V. A. R. Barão and W. G. Assunção, *Mater. Sci. Eng., C*, 2018, **92**, 849–861.
26 W. Wang, W. Cui, Z. Xiao and G. Qin, *Surf. Coat. Technol.*, 2022, 128415, DOI: **10.1016/j.surfcoat.2022.128415**.
27 C. Zhang, J. Huffer and M. Sprik, *J. Phys. Chem. Lett.*, 2019, **10**, 3871–3876.
28 W. Bao, Y. Wu, Y. Xie and C. Yao, *Funct. Mater. Lett.*, 2020, **13**, 2051017.
29 V. Puspasari, A. Ridhova, A. Hermawan, M. I. Amal and M. M. Khan, *Bioprocess Biosyst. Eng.*, 2022, **45**, 1421–1445.
30 V. Vibornijs, M. Zubkins, E. Strods, Z. Rudevica, K. Korotkaja, A. Ogurcovs, K. Kundzins, J. Purans and A. Zajakina, *Coatings*, 2023, **14**, 14.
31 M. M. Masadeh, N. M. Bany-Ali, M. S. Khanfar, K. H. Alzoubi, M. M. Masadeh and E. M. Al Momany, *Curr. Drug Delivery*, 2025, **22**, 92–106.